A Flow Control Study of a Simplified, Oscillating Truck Cabin Using PANS

(article starts on next page)

A Flow Control Study of a Simplified, Oscillating Truck Cabin Using PANS

G. Minelli[1]
Division of Fluid Dynamics,
Mechanics and Maritime Sciences,
Chalmers University of Technology,
Gothenburg 412 96, Sweden
e-mail: minelli@chalmers.se

S. Krajnović
Division of Fluid Dynamics,
Mechanics and Maritime Sciences,
Chalmers University of Technology,
Gothenburg 412 96, Sweden

B. Basara
Advanced Simulation Technologies,
AVL List GmbH,
Hans-List-Platz 1,
Graz 8020, Austria

This work presents an application of the partially averaged Navier–Stokes (PANS) equations for an external vehicle flow. In particular, the flow around a generic truck cabin is simulated. The PANS method is first validated against experiments and resolved large eddy simulation (LES) on two static cases. As a consequence, PANS is used to study the effect of an active flow control (AFC) on a dynamic oscillating configuration. The oscillation of the model represents a more realistic ground vehicle flow, where gusts (of different natures) define the unsteadiness of the incoming flow. In the numerical study, the model is forced to oscillate with a yaw angle $10 \deg > \beta > -10 \deg$ and a nondimensional frequency $St = fW/U_{inf} = 0.1$. The effect of the periodic motion of the model is compared with the quasi-static flow condition. At a later stage, the dynamic configuration is actuated by means of a synthetic jet boundary condition. Overall, the effect of the actuation is beneficial. The actuation of the AFC decreases drag, stabilizes the flow, and reduces the size of the side recirculation bubble. [DOI: 10.1115/1.4040225]

1 Introduction

Partially-averaged Navier–Stokes (PANS) [1,2] simulations have been successfully used for several different flow and heat transfer studies around ground vehicles and more generally bluff bodies [3,4]. Examples are the flow around a square-back Ahmed body [5], the flow around a simplified passenger vehicle influenced by crosswind [6,7], the flow around a landing gear [8], heat transfer applications [9,10], active flow control (AFC) applications for bluff bodies [11,12], and real vehicle flow studies [13,14]. The general conclusion is that PANS predictions of flows around simplified vehicles are in good agreement with the experimental observations. Furthermore, the PANS method captures the main features of an unsteady flow, with smaller computational effort when compared to large eddy simulation (LES). In fact, the idea behind hybrid methods, such as PANS, is to decrease the resolution requirement normally needed for LES. LES resolution is indeed very high in the near-wall regions, and this is where the PANS method is expected to activate more turbulence modeling and thereby decrease the computational effort. Thus, the PANS method used by the authors is based on the variable switching coefficient f_k, that regulates the amount of turbulence modeling in the simulation. In other words, the coarsening of the computational grid results in activation of more turbulence modeling, while a grid refinement allows the release of more turbulence scales. This normally leads to small differences in the time-averaged results when the grid refinement study is performed. Nonetheless, PANS remains a good engineering tool for unsteady flow predictions of ground vehicles. With this in mind, this method is used to study the flow and its actuation around a simplified truck cabin.

When studying ground vehicle aerodynamics one can observe that any area of separated flow (Fig. 1(*a*)) contributes to an aerodynamic drag increase and to a creation of noise and soiling on the side and rear windows [15]. At present, the control of turbulent boundary layer is still one of the main issue in fluid mechanics [16], and the ultimate goal of this ongoing project is to implement an effective AFC able to minimize the side recirculation bubble of a truck cabin, as shown in Fig. 1(*b*). Previous works of similar aerodynamic conditions have shown the effectiveness

of a flow control device, for both static stalled [17,18] and pitching [19,20] aerofoils. Studies on ground vehicle applications have approached this problem using different techniques, from suction and oscillatory blowing [21–23] to plasma actuators [24,25]. A preliminary LES [26] and experimental [27] works, show the effectiveness of flow control by means of synthetic jet actuation. In these two studies, an AFC was implemented both numerically and experimentally to reproduce the jet flow created by a moving membrane embedded at the A-pillar. An explanatory sketch is provided in Fig. 2(*b*). Following the same path, the implementation of a synthetic jet is applied to an oscillating model. Thus, this paper presents a prediction of a challenging vehicle flow condition. A three-dimensional bluff body, representative of a truck cabin, is oscillating with a yaw angle β. The unactuated configuration produces separation at the A-pillars, which is ultimately controlled by the synthetic jet actuation. The Reynolds number used in this study, based on the inlet velocity of 19.2 m/s and the width of the model $W = 0.4$ m, is $Re = 5 \times 10^5$. The oscillation of the model aims to reproduce a more realistic flow condition, where gusts, created by overtaking, atmospheric turbulence and cross wind, significantly influence the incoming flow. The use of an oscillating model to recreate realistic flow conditions was first explored in Ref. [28] and later investigated numerically and experimentally for a simplified car model in Refs. [29] and [30], respectively. Now, two parameters are chosen to define the oscillation of the model. The first one is the oscillation frequency, chosen as $St = fW/U_{inf} = 0.1$, and the second one is the yaw angle range $10 \deg > \beta > -10 \deg$. These choices are supported by "on road" experiments [31–33], which highlight the range of important frequencies in cross wind studies between $0.09 > St > 0.9$ and a most common lateral wind speed of about 4–5 m/s [31] which, in particular, leads to the choice of the yaw angle range. In conclusion, the main objectives of this paper are listed below:

- PANS is validated to be a good engineering tool for unsteady flow prediction.
- The continuous yawing configuration is compared with the quasi-static condition. The flow structures are compared and analyzed highlighting the effect of the oscillation of the model.
- An active flow control is introduced to stabilize the separation during the yawing, to enhance the aerodynamic performance and to reduce the side recirculation bubbles.

The remainder of the paper is organized as follows: Sec. 2 details the numerical setup and formulation. Section 3 is divided
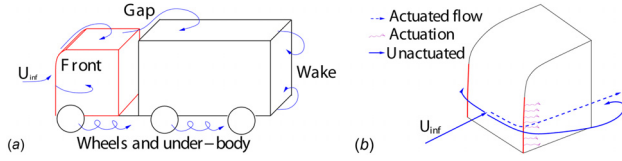

Fig. 1 A sketch of the separated flow regions of a truck: (*a*) the main sources of aerodynamic drag and (*b*) the A-pillar separation and the effect of the actuation
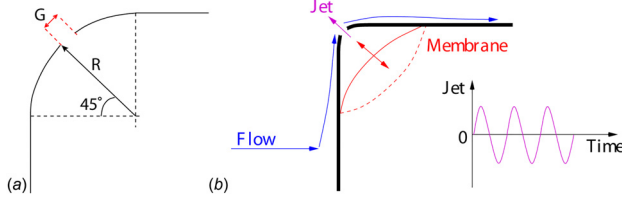

Fig. 2 The slot that defines the AFC: (*a*) the slot location and (*b*) a sketch of the jet flow by means of a membrane motion

into three main parts: first, the results regarding the validation of PANS compared to resolved LES results are presented; second, the quasi-static numerical solutions are compared with the dynamic results; third, an AFC application is simulated under dynamic oscillatory conditions. Conclusions are presented in Sec. 4.

2 Numerical Setup

Partially-averaged Navier–Stokes were employed for the numerical study of the AFC, while LES was used for a more complete validation of the first method. The numerical domain presented in Fig. 3 was used and the following boundary conditions. A homogeneous Neumann boundary condition was applied at the outlet. The surfaces of the body and the wind tunnel walls were treated as no-slip walls. A time varying velocity, Eq. (20), reproduced the jet flow described by Fig. 2(*b*). This figure shows how the motion of a membrane (e.g., a loud-speaker membrane) creates a periodic jet flow at the slot. When the flow is unactuated, the AFC surface was defined as a no-slip wall, likewise the rest of the body. The position of the actuator and the slot dimension are described by Fig. 2(*a*) and Table 1, respectively. The oscillation of the model around the vertical axis was obtained by deforming the computational grid. The deformation of the grid was made only in a circular region around the model (within a nondimensional radius $R_{\mathrm{def}}/W = 2.5$). The simulations in this work are made with the commercial finite volume CFD solver, AVL FIRE [34]. AVL FIRE is based on the cell-centered finite volume approach.

2.1 Resolution and Numerical Schemes. Pope [35] suggested that a reliable LES grid should resolve 80% of the turbulent energy. In order to achieve this and resolve the near wall turbulent structures of the flow, the first grid point in the wall normal direction must be located at $n^+ < 1$, where $n^+ = ((u_\tau n)/\nu)$ with
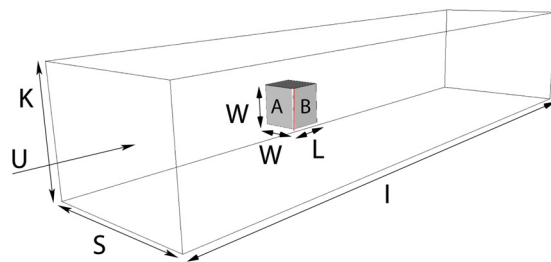
Table 1 Dimension of the computational domain

G	L	I	K	S	R
0.0025	0.9	17.5	3	4.5	0.05

Note: All dimensions are scaled by the model width $W = 0.4$ m.

the friction velocity u_τ, while the resolutions in the spanwise and streamwise directions must be $\Delta l^+ \simeq 15 - 40$ and $\Delta s^+ \simeq 50 - 150$, respectively [36]. Here, $\Delta l^+ = ((u_\tau \Delta l)/\nu)$ and $\Delta s^+ = ((u_\tau \Delta s)/\nu)$. In this work, the grid resolution has an average value in the wall normal direction of $n^+ = 0.45$ and a maximum value of $n^+ = 1.7$ only at the sharp edges of the rear end of the model. The resolutions in the spanwise and streamwise directions are reported in Table 2. The number of computational cells of the PANS grid has been reduced by 75%, as compared to the LES grid. The coarsening procedure affects only the spanwise and streamwise directions (z and y directions). The chosen time-step, $\Delta t^* = \Delta t U_{\mathrm{inf}}/W$, is $\Delta t^* = 9.6 \times 10^{-4}$ for all simulations, resulting in a CFL number lower than 1 in the entire domain. All simulations were run first until the flow was fully developed. This was followed by an averaging of $t^* = t U_{\mathrm{inf}}/W = 20$. For LES, the convective fluxes are approximated by a blend of 96% linear interpolation of second-order accuracy (central differencing scheme) and of 4% upwind differences of first-order accuracy (upwind scheme). In PANS, a second-order upwind scheme AVL SMART Bounded [37] was used to approximate the convective fluxes for the momentum equation in conjunction with the second-order bounded MINMOD scheme [38,39] for the equations describing the turbulence closure system. The time marching procedure is done using the implicit second-order accurate three-time level scheme.

2.2 The Partially-Averaged Navier–Stokes Equations. The PANS governing equations are defined by the following model [1,40]:

$$\frac{\partial U_i}{\partial x} = 0 \tag{1}$$

$$\frac{\partial U_i}{\partial t} + U_j \frac{\partial U_i}{\partial x_j} = -\frac{1}{\rho}\frac{\partial p}{\partial x_i} + \frac{\partial}{\partial x_j}\left(\nu \frac{\partial U_i}{\partial x_j} + \tau(V_i, V_j)\right) \tag{2}$$

where $\tau(V_i, V_j)$ is the generalized second moment [41] and represents the effect of the unresolved scales on the resolved field. The Boussinesq assumption is now invoked to model the second moment

$$\tau(V_i, V_j) = -2\nu_u S_{ij} + \frac{2}{3}k_u \delta_{ij} \tag{3}$$

Here, k_u is the unresolved kinetic energy, $S_{ij} = (1/2)(\partial U_i/\partial x_j + \partial U_j/\partial x_i)$ is the resolved stress tensor, and $\nu_u = C_\mu \zeta_u k_u^2/\varepsilon_u$ is the viscosity of the unresolved scales, where $\zeta = \overline{v_u^2}/k_u$ is the velocity scale ratio of the unresolved velocity scale $\overline{v_u^2}$ and unresolved turbulent kinetic energy k_u. $\overline{v_u^2}$ refers to the normal fluctuating component of the velocity field to any no-slip boundary. At this stage,

Table 2 Details of the computational grids

Case	Fine LES grid	Coarse PANS grid
Number of cell	16×10^6	4×10^6
y^+_{mean}	<0.5	<0.5
$\Delta s^+_{\mathrm{max}}$	<100	<450
$\Delta l^+_{\mathrm{max}}$	<100	<450
$\Delta s^+_{\mathrm{mean}}$	<35	<120
$\Delta l^+_{\mathrm{mean}}$	<35	<120

Fig. 3 The numerical domain

three transport equations for k_u–ε_u–ζ_u and a Poisson equation for the elliptic relaxation function of the unresolved velocity scales are necessary to close the model. Thus, the complete PANS k–ε–ζ–f model is given by the following set of equations:

$$\frac{\partial k_u}{\partial t} + U_j \frac{\partial k_u}{\partial x_j} = P_u - \varepsilon_u + \frac{\nu_u}{\sigma_{k_u}} \frac{\partial^2 k_u}{\partial x_j^2} \tag{4}$$

$$\frac{\partial \varepsilon_u}{\partial t} + U_j \frac{\partial \varepsilon_u}{\partial x_j} = C_{\varepsilon 1} P_u \frac{\varepsilon_u}{k_u} - C_{\varepsilon 2}^* \frac{\varepsilon_u^2}{k_u} + \frac{\nu_u}{\sigma_{\varepsilon_u}} \frac{\partial^2 \varepsilon_u}{\partial x_j^2} \tag{5}$$

$$\frac{\partial \zeta_u}{\partial t} + U_j \frac{\partial \zeta_u}{\partial x_j} = f_u - \frac{\zeta_u}{k_u} (\varepsilon_u (1 - f_k) - P_u) + \frac{\nu_u}{\sigma_{\zeta_u}} \frac{\partial^2 \zeta_u}{\partial x_j^2} \tag{6}$$

$$L_u^2 \nabla^2 f_u - f_u = \frac{1}{T_u} \left(c_1 + c_2 \frac{P_u}{\varepsilon_u} \right) \left(\zeta_u - \frac{2}{3} \right) \tag{7}$$

$\nu_u = C_\mu \zeta_u (k_u^2 / \varepsilon_u)$ is the unresolved turbulent viscosity. $P_u = -\tau(V_i, V_j)(\partial U_i / \partial x_j)$ is the production of the unresolved turbulent kinetic energy, which is closed by the Boussinesq assumption, Eq. (3). The coefficients $C_{\varepsilon 2}^*$ and $C_{\varepsilon 1}$ are defined as

$$C_{\varepsilon 2}^* = C_{\varepsilon 1} + f_k (C_{\varepsilon 2} - C_{\varepsilon 1}) \tag{8}$$

$$C_{\varepsilon 1} = 1.4 \left(1 + \frac{0.045}{\sqrt{\zeta_u}} \right) \tag{9}$$

$\sigma_{k_u} = \sigma_k (f_k^2 / f_\varepsilon)$ and $\sigma_{\varepsilon_u} = \sigma_\varepsilon (f_k^2 / f_\varepsilon)$ are the counterpart of the unresolved kinetic energy and dissipation, respectively. In this way, f_k and f_ε contribute to changing the turbulent transport Prandtl number contributing to the decrease of the unresolved eddy viscosity [42]. The constants appearing in Eqs. (4)–(7) are: $C_\mu = 0.22$, $C_{\varepsilon 2} = 1.9$, $c_1 = 0.4$, $c_2 = 0.65$, $\sigma_k = 1$, $\sigma_\varepsilon = 1.3$, $\sigma_{\zeta_u} = 1.2$. L_u and T_u are the length and time scales defined by using the unresolved kinetic energy

$$T_u = \max \left[\frac{k_u}{\varepsilon}, C_\tau \left(\frac{\nu}{\varepsilon} \right)^{1/2} \right] \tag{10}$$

$$L_u = C_L \max \left[\frac{k_u^{3/2}}{\varepsilon}, C_\delta \left(\frac{\nu^3}{\varepsilon} \right)^{1/4} \right] \tag{11}$$

where $C_\tau = 6$, $C_L = 0.36$, and $C_\delta = 85$. A more detailed explanation of the construction of the equations is given in Refs. [2] and [43].

The parameters $f_{k,\varepsilon}$ are the key factors that make the model act dynamically. $f_{k,\varepsilon}$ are the ratios between resolved to total kinetic energy and dissipation, respectively, and they can assume values between 1 and 0 according to the selected cutoff. These parameters can be chosen a priori, knowing the resolution of the given grid. However, it might be more efficient to have a solver that adapts its accuracy to the flow case and the given grid, having as its worse output a RANS simulation. Here is indicated the importance of having a dynamic parameter that feels the characteristics of both the flow and the grid, adapting to the resolvable level of structures. For a further but justified simplification, f_ε is assumed to be constant and equal to 1. We recall the spatial resolution to resolve the dissipative scales, and the inertial sub-range is a near wall DNS resolution. These scales are unlikely to be resolved in most cases. Thus, all the unresolved dissipation is chosen to be RANS dissipation and is therefore modeled. Thus, the crucial step to developing an efficient model is the design of the last parameter f_k. Ideally, at every time-step for every computational cell, the simulation should measure the smallest value of f_k which the grid can support. Using this approach, the dynamic parameter was proposed as the ratio between the geometric-averaged grid cell

dimension, $\Delta = (\Delta_x \Delta_y \Delta_z)^{1/3}$, and the Taylor scale of turbulence, $\Lambda = (((k_u + k_{res})^{3/2}) / \varepsilon)$ for the first time in Ref. [44]

$$f_k(x, t) = \frac{1}{\sqrt{C_\mu}} \left(\frac{\Delta}{\Lambda} \right)^{2/3} \tag{12}$$

2.3 The Large Eddy Simulation Equations. The governing LES equations are the spatially implicitly filtered Navier–Stokes equations, where the spatial filter is determined by the characteristic width $\Delta = (\Delta_1 \Delta_2 \Delta_3)^{(1/3)}$, and Δ_i is the computational cell size in the three coordinate directions

$$\frac{\partial \overline{u}_i}{\partial x_i} = 0 \tag{13}$$

and

$$\frac{\partial \overline{u}_i}{\partial t} + \frac{\partial}{\partial x_j} (\overline{u}_i \overline{u}_j) = -\frac{1}{\rho} \frac{\partial \overline{p}}{\partial x_i} + \nu \frac{\partial^2 \overline{u}_i}{\partial x_j \partial x_j} - \frac{\partial \tau_{ij}}{\partial x_j} \tag{14}$$

Here, $\overline{u}_i$ and $\overline{p}_i$ are the resolved velocity and pressure, respectively, and the bars over the variables denote the operation of filtering. The influence of the small scales in Eq. (14) appears in the sub-grid scale (SGS) stress tensor, $\tau_{ij} = \overline{u_i u_j} - \overline{u}_i \overline{u}_j$. The algebraic eddy viscosity model, described in Ref. [45], was employed in this work. The Smagorinsky model represents the anisotropic part of the SGS stress tensor, τ_{ij} as

$$\tau_{ij} - \frac{1}{3} \delta_{ij} \tau_{kk} = -2 \nu_{sgs} \overline{S}_{ij} \tag{15}$$

where the SGS viscosity

$$\nu_{sgs} = (C_s f_{vd} \Delta)^2 |\overline{S}| \tag{16}$$

and

$$\overline{S} = \sqrt{(2 \overline{S}_{ij} \overline{S}_{ij})} \tag{17}$$

where

$$\overline{S}_{ij} = \frac{1}{2} \left(\frac{\partial \overline{u}_i}{\partial x_j} + \frac{\partial \overline{u}_j}{\partial x_i} \right) \tag{18}$$

The Smagorinsky constant, $C_s = 0.1$, previously used in bluff body LES [46], is used in this work. f_{vd}, in Eq. (16), is the Van Driest damping function

$$f_{vd} = 1 - \exp \left(\frac{-n^+}{25} \right) \tag{19}$$

where n^+ is the wall normal distance in viscous units.

2.4 Actuation's Parameters. The magnitude of the velocity at the actuation region (G in Fig. 2(a)), U_{afc}, was defined by the time varying boundary condition as follows:

$$U_{afc} = 0.26 U_{inf} \sin(t 2 \pi f_a) \tag{20}$$

where U_{inf} is the magnitude of the freestream velocity, and $f_a = 150\,\text{Hz}$ is the actuation frequency. Two nondimensional parameters describe the performance of the actuation. The first parameter is the momentum coefficient, C_η. This is an indicator of the energy spent for the actuation ($\overline{I}_j$) with respect to the energy of the unactuated flow

$$\bar{I}_j = \left(\frac{2}{T}\right)\rho_j G \int_0^{T/2} U_{\text{afc}}^2(t)dt \qquad (21)$$

$$C_\eta = \frac{\bar{I}_j}{\frac{1}{2}\rho W U_{\text{inf}}^2} \qquad (22)$$

Here, $\rho_j = \rho$ is the flow density, and T is the actuation period. $C_\eta = 1.22 \times 10^{-4}$ is low but sufficient to excite the thin boundary layer that characterizes the attached flow before its separation. All the frequencies in this work are described in terms of the second nondimensional parameter, the reduced frequency F^+

$$F^+ = \frac{f_a}{U_{\text{inf}}/W} \qquad (23)$$

Here, f_a represents the actuation frequency in Hertz. In this work $F^+ = 3.1$.

3 Results and Discussion

An extensive validation of the PANS method for the static configuration is reported in Ref. [12]. In the mentioned study, PANS results are compared against resolved LES simulations and experimental particle image velocimetry data. As a continuation of the previous work, the dynamic PANS simulation is compared in this paper with dynamic resolved LES results. After the validation procedure, the PANS method was further used to compare the effect of the periodic oscillation of the model to the static condition. At last, the introduction of a flow control strategy is applied. In particular Fig. 4 shows the location and the description of the slot producing the synthetic jet actuation.

3.1 Partially-Averaged Navier–Stokes Validation.

Dynamic simulations have been run for both PANS and LES. Velocity was probed in specific locations (see Fig. 5) during the simulations.
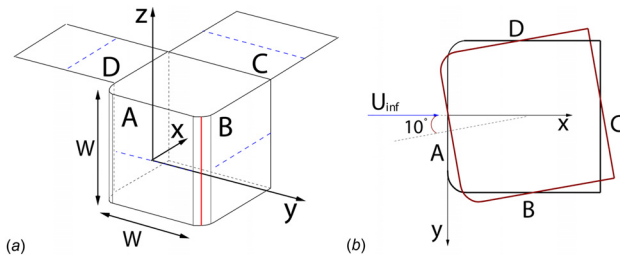

Fig. 4 A sketch of the model used in this study. (a) A three-dimensional representation of the simplified truck cabin. The red line indicates the AFC position, the blue dashed lines indicate location of the pressure tabs. (b) A top view of the model; two configurations at β = 0 deg and β = 10 deg.
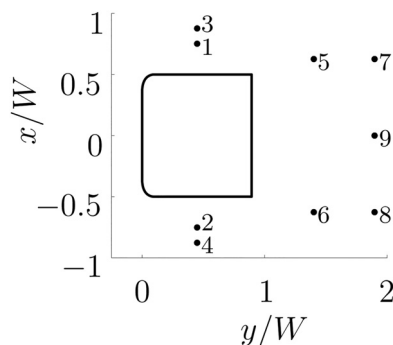

Fig. 5 Probing points located on the horizontal plane z = 0 (model centerline). Flow from left to right.
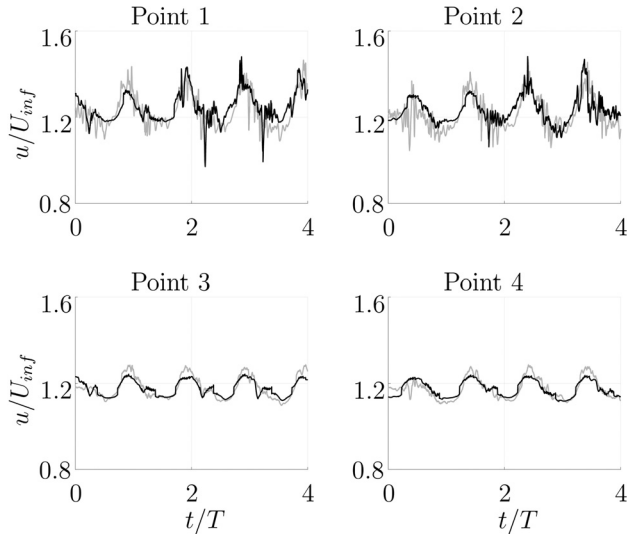

Fig. 6 Time history of four points located in the side recirculation bubble (for points' locations refer to Fig. 5). LES gray and PANS black. T corresponds to one complete oscillation period.

Figures 6 and 7 show that PANS and LES velocity time history signals match for all probed locations, both in the side recirculation bubble, Fig. 6, and in the wake region, Fig. 7. Nevertheless, LES shows a more complicated signal characterized by a larger range of oscillations. In particular, the comparison of the fast Fourier transform (FFT) analysis of two probed signals, presented in Fig. 8, shows clearly a wider range of peaks when the LES calculation is considered (gray solid lines). This is also corroborated by Fig. 9 which compares the multitude of structures resolved by LES. As visible, PANS is capable of resolving only large structures present in the flow, while LES captures finer eddies that define, for example, the separated flow. Wake spectra of the turbulent kinetic energy are commonly computed to find out whether they exhibit a –5/3 behavior. This method is used to verify the resolution of the computed mesh and if the turbulence structures are well captured by the computation. Following this, both the unactuated and actuated PANS cases are also compared with the wake spectrum obtained from LES and Fig. 10 shows that the $-5/3$ turbulence decay slope is well captured by the coarse PANS
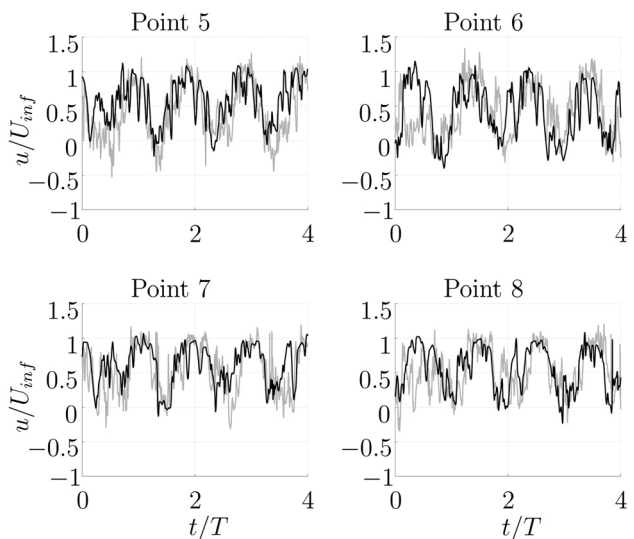

Fig. 7 Time history of four points located in the wake (for points' locations refer to Fig. 5). LES gray and PANS black. T corresponds to one complete oscillation period.
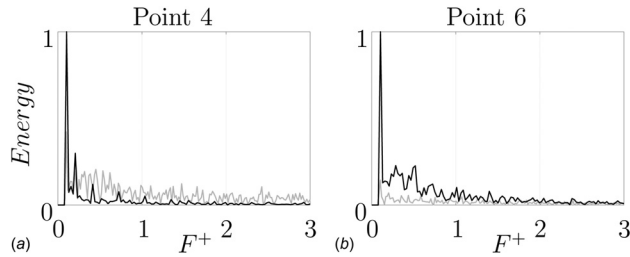
Fig. 8 Fast Fourier transform (FFT) spectra for PANS (black) and LES (gray). Point 4 (*a*) and point 6 (*b*) (for points' locations refer to Fig. 5).
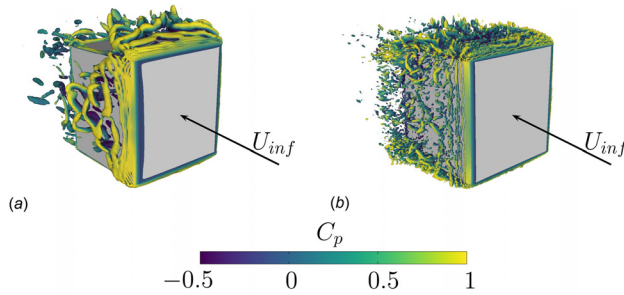

Fig. 9 Isosurface of the second invariant of the velocity colored by the streamwise flow velocity. PANS (*a*) and LES (*b*) dynamic simulations. $\beta = 5$ deg clockwise rotation.

Fig. 11 Forces values comparison: (*a*) C_d and (*b*) C_s. Static simulations values are represented with dots and dynamic unactuated simulation values with solid lines. LES results are shown in gray and PANS results in black.

is applied. Overall, PANS is shown to capture the main features of the flow and to produce reliable results for such a challenging case.

calculations. The drag C_d and side force C_s coefficients are also compared with LES for a complete validation. Figure 11 shows both the hysteresis of the coefficients of the dynamic case (solid lines) and the comparison of two static cases (dots). In the dynamic configuration, the coefficients were phase averaged over four oscillation periods. This could explain the nonperfect match between the hysteresis of LES and PANS coefficients. Nevertheless, the values are in the same range and the behavior of the hysteresis is similar in both calculations. Concerning the static cases (dots in Fig. 11), the zero yaw case gives values in good agreement between the fine LES and the coarse PANS. Nonappreciable discrepancies are observed in terms of forces, and the difference between the two calculations remains within 1%. More challenging is the prediction of the $\beta = 10$ deg case. In this case, the severe separation at the leeward side is well captured by PANS. On the other hand, considering the windward separation, PANS predicts a larger separated region, while the pressure value of the base is under-predicted. The consequence is that PANS over-predicts the LES value by a 3% when $\beta = 10$ deg (the mentioned over-prediction of the pressure values is reported in Ref. [12], Fig. 6). However, this value can be still considered acceptable for the qualitative analysis of this study that aims to observe drag reduction and recirculation bubble suppression, once active flow control
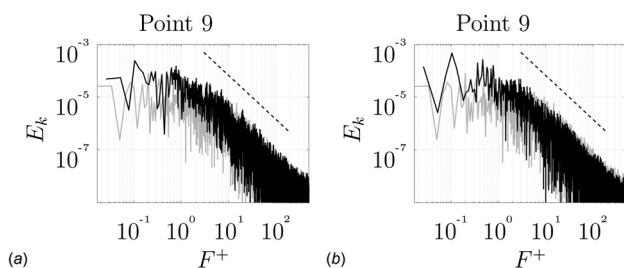
3.2 Quasi-Static Versus Dynamic Case. A static study of three different yawed configurations, between 0 deg and 10 deg, is reported and compared with the dynamic study of the flow. Figures 12–14 show the difference in the flow structures between the static and the dynamic configurations at the same yaw angle. The fluctuations introduced by the periodic movement of the model enhance the aerodynamic performance. The separated region appears reduced in the dynamic case, where smaller and less organized structures characterize the wake. As an example, the static configuration presented in Fig. 14(*b*) shows a recursive and regular separation at the leeward side. This separation is not visible for the dynamic case, where the oscillation of the model breaks the larger and well-organized structures. The result of this is a chaotic formation of eddies that does not have time to develop and organize a large recirculation bubble. In fact, observing the static case, the side separated flow merges into the wake for both $\beta = 5$ deg and $\beta = 10$ deg (Figs. 13(*a*) and 14(*a*), respectively). On the contrary, for the oscillating case, the side-separated flow does not directly interact with the wake and, in particular, often tends

Fig. 10 Turbulent kinetic energy E_k spectra at points 9 (for point's location refer to Fig. 5). LES gray and PANS black: (*a*) LES against unactuated PANS case and (*b*) LES against actuated PANS case. The dashed line shows the −5/3 slope.
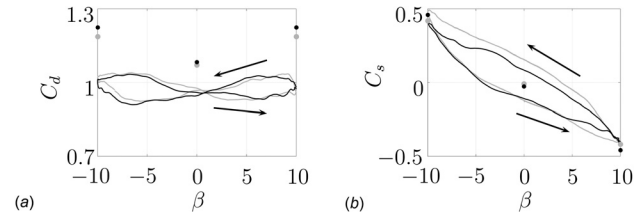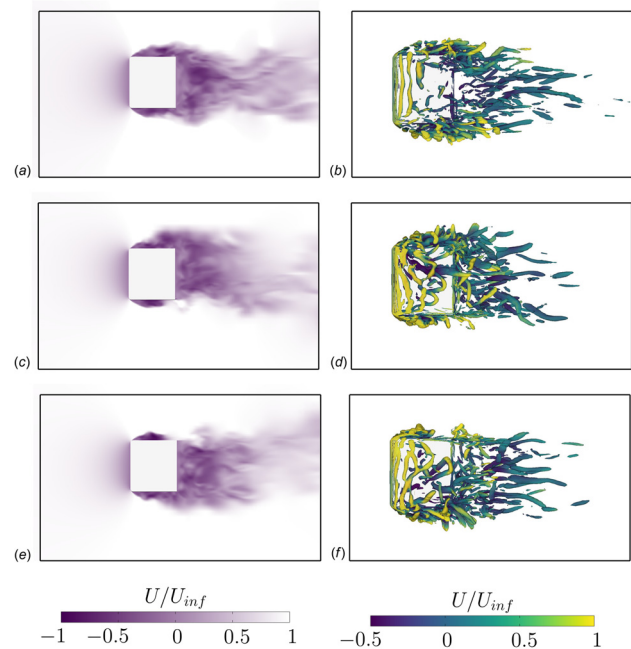

Fig. 12 Instantaneous streamwise flow velocity (*a*), (*c*), and (*e*) and isosurfaces of the second invariant of the velocity colored by the streamwise flow velocity (*b*), (*d*), and (*f*). The static (*a*) and (*b*), the dynamic configuration at $\beta = 0$ deg during a counter clockwise (positive) rotation (*c*) and (*d*) and a clockwise (negative) rotation (*e*) and (*f*).
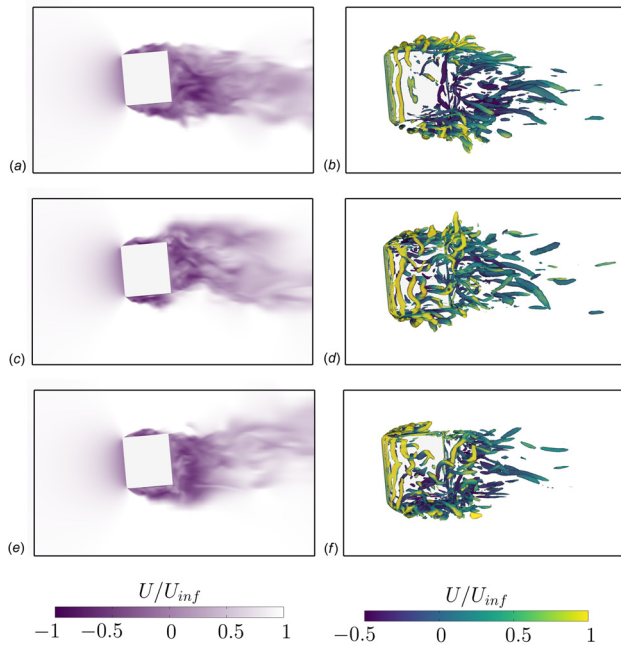
Fig. 13 Instantaneous streamwise flow velocity (a), (c), and (e) and isosurfaces of the second invariant of the velocity colored by the streamwise flow velocity (b), (d), and (f). The static (a) and (b) and the dynamic configuration at $\beta = 5$ deg during a counter clockwise (positive) rotation (c) and (d) and a clockwise (negative) rotation (e) and (f).

to reattach at the rear end of the model, Figs. 13(c), 13(e), and 14(c). This behavior explains the reduction of the drag. In particular, Fig. 11(a) shows the overall reduction of the aerodynamic drag for the dynamic case when compared to the quasi-static configuration. As mentioned before, the oscillation mitigates the pronounced separation observed in the quasi-static configuration, decreasing the coefficient of drag C_d for every yaw angle, while the side force coefficient C_s remains in the same range for both configurations. The introduction of the oscillation also creates the hysteresis effect visible in Fig. 11 (solid lines). When the model is forced to a solid movement, the surrounding flow tends to follow the rotation, experiencing an inertial effect (which leads to the hysteresis) when the rotation changes sign. This phenomenon is documented by Figs. 12–14. Figures 12(c) and 12(e) represent the
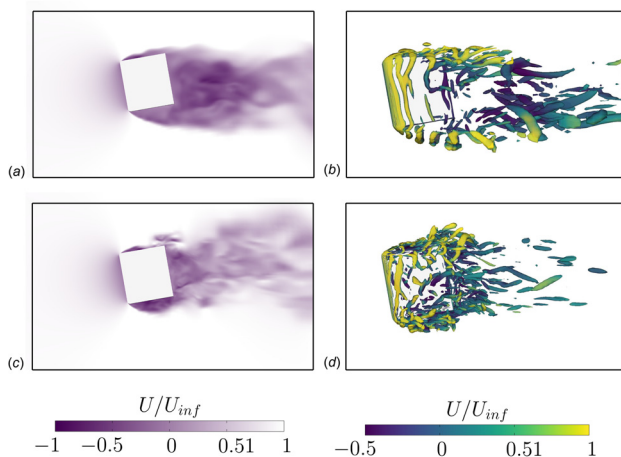

Fig. 14 Instantaneous streamwise flow velocity (a) and (c) and isosurfaces of the second invariant of the velocity colored by the streamwise flow velocity (b) and (d). The static (a) and (b) and the dynamic (c) and (d) configuration at $\beta = 10$ deg.
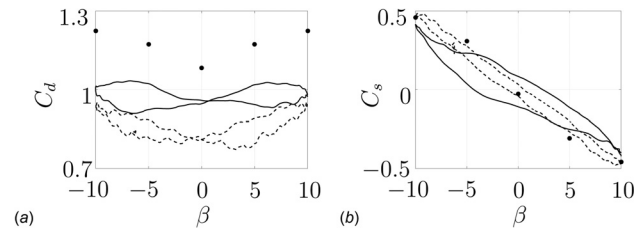
Fig. 15 Forces values comparison: C_d (a) and C_s (b). Static simulations values are represented with dots and dynamic unactuated simulation values with solid lines. The dynamic actuated simulation results are shown using dashed lines.

model at $\beta = 0$ deg during a counter clockwise (positive) and a clockwise (negative) rotation, respectively, while Figs. 13(c) and 13(e) show the flow instant when $\beta = 5$ deg during a positive and a negative rotation, respectively. In both cases, the inertial effect of the rotation sign change, is clearly visible. The wake is never aligned to the model, as it was for the static case, and the flow at the leeward side almost reattaches at the rear end of the body. Moreover, as shown in Fig. 13(e), the sign change has just occurred, and the inertia of the flow enlarges the already pronounced separation at the leeward side. Looking at the structures visualized in Figs. 13(d) and 13(f), one can notice the strong agglomeration of eddies at the leeward side when a negative rotation has just finished (Fig. 13(f)), while the eddies are more evenly distributed toward the end of a positive rotation period (Fig. 13(d)). The same inertial behavior, and the consequent agglomeration of eddies, is still present when the rotation (positive depicted in Fig. 12(d) and negative reported in Fig. 12(f)) is in the middle of its period. The counter-clock and clockwise rotation, obviously, give the opposite inertial effect to the wake that is pulled periodically toward the opposite direction of the rotation. Observing this first comparison, it is clear that a gusty flow condition (formed by the oscillation of the model) produces a fundamentally different flow from the quasi-static configuration. Thus, it is of major
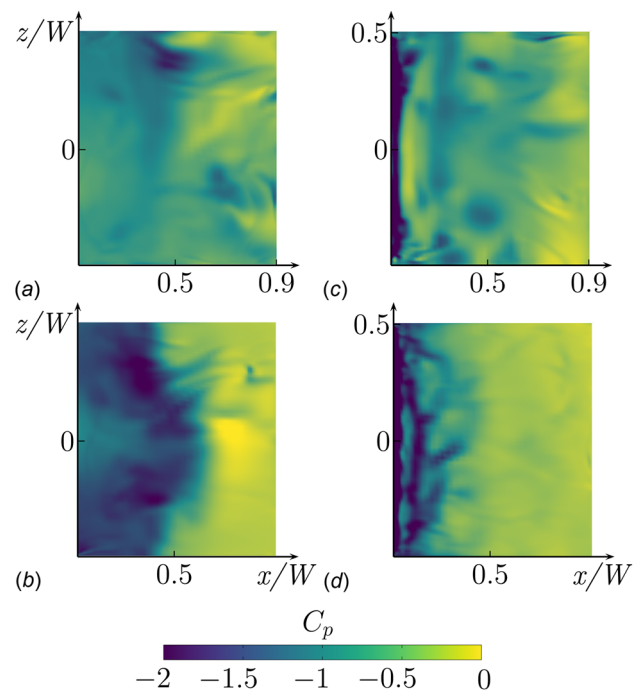

Fig. 16 C_p on the side faces D and B of the model (refer to Fig. 4). Instantaneous C_p on D (a) and B (b) faces (instant presented in Fig. 19(a)), unactuated case. Instantaneous C_p on D (c) and B (d) faces (instant presented in Fig. 19(f)), actuated case.

importance to investigate and understand the possibilities of an AFC under this flow condition.

3.3 Unactuated Versus Actuated Case. Active flow control is applied to the A-pillar of the oscillating model in order to stabilize the flow, minimize the hysteresis effect, and reduce the recirculation bubble. The ultimate goal is to observe drag reduction during the rotation of the model. The plot depicted in Fig. 15(*a*) shows drag signals of quasi-static (dots), dynamic unactuated (solid line), and dynamic actuated (dashed line) cases. From a first look, one can observe a small reduction of the hysteresis and a consistent reduction of drag when the flow is actuated for all yaw angles. In particular, drag is reduced by a maximum of 18%, when $\beta = \pm 2.5$ deg, to a minimum of 4%, when $\beta = \pm 10$ deg, producing a mean value of 10.5% of drag reduction during one complete oscillation.

Attention should be also paid to the behavior of the side force coefficient C_s, shown in Fig. 15(*b*). In this case, the hysteresis has been almost suppressed by the introduction of the AFC, indicating a more homogeneous flow on both sides during one complete sweep. This can be interpreted as a positive effect on the stability of the model. In general, the inertial effect of the flow is mitigated and stabilized, having, in contrast to the unactuated case, almost no side force at $\beta = 0$ deg. On the other hand, it is also clear that the actuation is not able to recover the heavily separated flow at the leeward side, when the yaw angle increases. In fact, the plot of the side force of the actuated case follows the quasi-static side force measurement trend (dashed line and dots shown in Fig. 15(*b*), respectively). Figure 16 corroborates and clarifies the side force behavior so far described. Figures 16(*a*) and 16(*b*) shows the instantaneous coefficient of pressure (unactuated case) on D and B faces, respectively, at $\beta = 0$ deg, during a counter-clockwise rotation. The C_p is fundamentally different from one face to the other. On the leeward side (see Fig. 16(*b*)) the separation and reattachment of the flow are clear and strong, and the averaged value of the pressure coefficient on this face is $C_{p,\text{mean}} = 0.97$. On the windward side (see Fig. 16(*a*)), instead, the C_p variation is
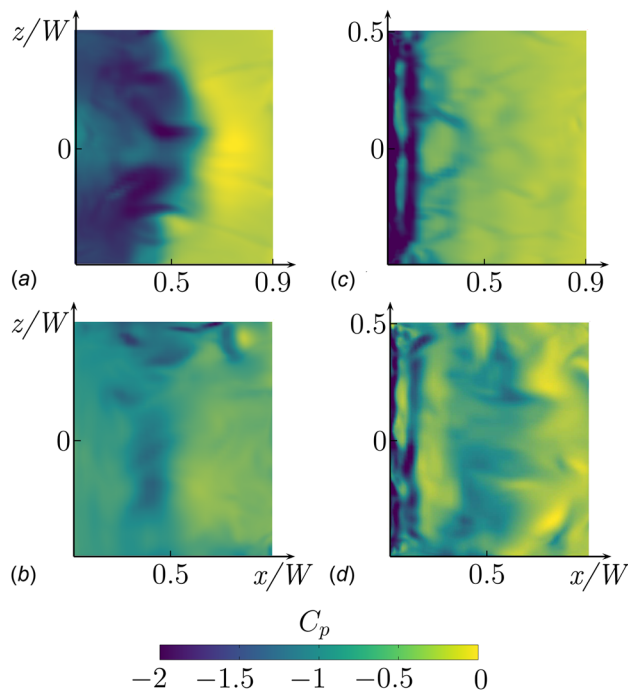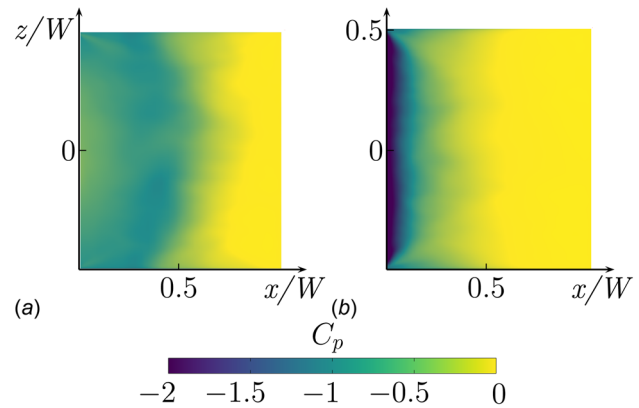

Fig. 18 Averaged C_p on D face (refer to Fig. 4) over four complete oscillations: (*a*) unactuated case and (*b*) actuated case

weaker, and its value is more homogeneous over the surface, with a $C_{p,\text{mean}} = 0.83$. The result is a large difference in the mean value of the pressure force acting on each face, which brings an explanation to a nonzero side force for $\beta = 0$ deg, when the flow is unactuated (see Fig. 15(*b*)). On the contrary, Figs. 16(*c*) and 16(*d*) shows a more similar pressure distribution on both faces D (Fig. 16(*c*)),
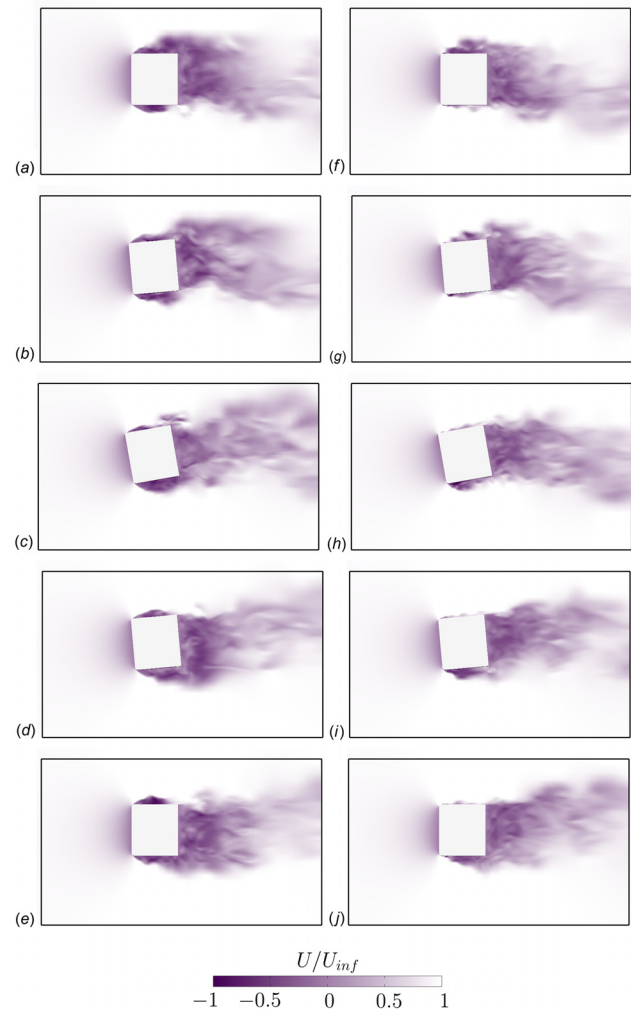

Fig. 17 C_p on the side faces D and B of the model (refer to Fig. 4). Instantaneous C_p on D (*a*) and B (*b*) faces (instant presented in Fig. 19(*e*)), unactuated case. Instantaneous C_p on D (*c*) and B (*d*) faces (instant presented in Fig. 19(*l*)), actuated case.

Fig. 19 Instantaneous streamwise flow velocity: unactuated (*a*)–(*e*) and actuated (*f*)–(*l*) case. From top: $\beta = 0$ deg counter clockwise rotation (*a*) and (*f*), $\beta = 5$ deg counter clockwise rotation (*b*) and (*g*), $\beta = 10$ deg (*c*) and (*h*), $\beta = 5$ deg clockwise rotation (*d*) and (*i*), $\beta = 0$ deg clockwise rotation (*e*) and (*l*).

Fig. 20 Isosurface of the second invariant of the velocity colored by the streamwise flow velocity. Unactuated (*a*)–(*e*) and actuated (*f*)–(*l*) case. From top: $\beta = 0$ deg counter clockwise rotation (*a*) and (*f*), $\beta = 5$ deg counter clockwise rotation (*b*) and g), $\beta = 10$ deg (*c*) and (*h*), $\beta = 5$ deg clockwise rotation (*d*) and (*i*), $\beta = 0$ deg clockwise rotation (*e*) and (*l*).
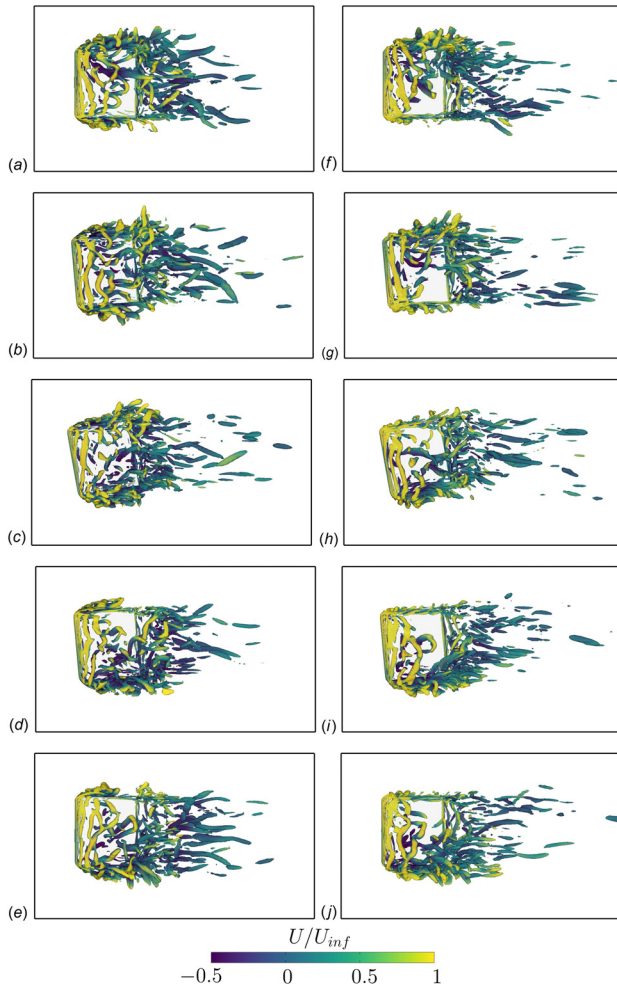

Fig. 21 Isosurface of the second invariant of the velocity colored by the streamwise flow velocity. Unactuated (*a*) and actuated (*b*) cases. $\beta = 5$ deg clockwise rotation.

Fig. 22 FFT spectra for unactuated (solid) and actuated (dashed) cases: (*a*) Point 4, and (*b*)point 6 (for points' locations refer to Fig. 5)

with a $C_{p,\mathrm{mean}} = 0.80$, and B (Fig. 16(*d*)), with a $C_{p,\mathrm{mean}} = 0.75$. The very similar mean C_p values explain the reduction of the side force to zero for $\beta = 0$ deg, when the flow is actuated. Comparing Figs. 16(*a*)–16(*b*) and 17(*a*)–17(*b*), one can notice that at $\beta = 0$ deg the C_p distribution inverts sides, from a positive (counter clockwise), shown in Fig. 16, to a negative, shown in Fig. 17, rotation of the model. In contrast to that, the swapping of the side pressure map, due to the change of the rotation sign, is still visible but mitigated when the flow is actuated, Figs. 16(*c*), 16(*d*), 17(*c*), and 17(*d*). Overall, the pressure recovery, operated by the AFC, is clearly visible. Indeed, the time-averaged pressure distribution on the side face over four complete sweeps, depicted in Fig. 18, shows a shorter recirculation bubble in favor of the actuated case. This is reflected in the drag coefficient reduction, previously visualized in Fig. 15.

Now, in an ideal case, the AFC should suppress both side separations, reducing to the minimum drag and side force effects. Further studies needs to be conducted to verify the possibility to suppress both side separations, also in extreme conditions (gusty wind). To conclude, Figs. 19–21 compare the flow field and flow structures before and after the introduction of the AFC, during a positive and a negative rotation. As stressed before, it is more challenging to manipulate the flow on the leeward side, where the separation is more pronounced. Nonetheless, the leeward separation is controlled to some extent by the AFC, and in addition, the
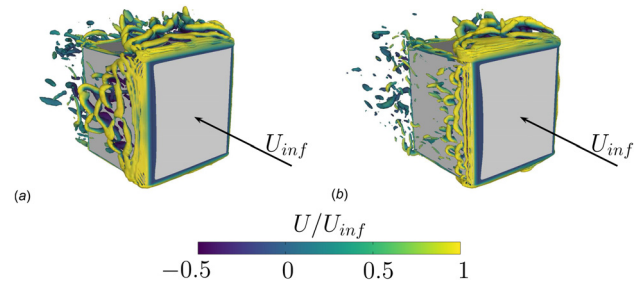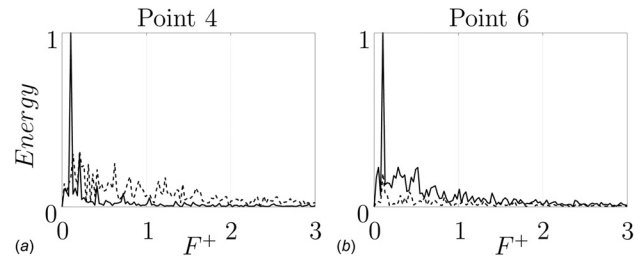
windward side separation is always suppressed, as highlighted by Fig. 21. Illustrated in more detail, Figs. 19 and 20 (*c*) and (*h*) show a notable reduction of the separated flow on the leeward side, and a stronger deflection of the shear layer toward the surface of the body (*h*). Figure 20 also shows a general, notable decrease of eddies formed at the A-pillar separation, when the flow is actuated, indicating a more stable flow around the model.

It is also of interest to look into how the actuation modifies the surrounding flow and eventually suppresses the wind gusts impinging the truck cabin. The FFT plots of two probed velocity signals probed by points surrounding the model are shown and computed in Fig. 22. Both signals are normalized by the maximum peak of the unactuated flow case signal. In this way, the mentioned plots show the reduction of the peak representing the oscillation frequency of the model ($F^+ = 0.1$) in favor of more evenly distributed energy spectra (dashed line) when the actuation is applied. In other words, the dominant frequency created by the wind gusts is mitigated by the AFC also in the surrounding flow.

4 Conclusions

This work shows the potential of the PANS method when employed to simulate challenging, unsteady flow conditions. In particular, the case studied here presents two challenging features. The first consists of the dynamic oscillation of the truck cabin between -10 deg $< \beta < 10$ deg, achieved by deforming the mesh around the solid model. The second one is the implementation of a sinusoidal inlet boundary condition, which reproduces the suction and blowing of a synthetic jet actuator. The PANS method was first validated for the static flow conditions, and then, the same method was employed to study the quasi-static, dynamic, and dynamic-actuated flow conditions. The following goals are achieved in the study:

- The potential of PANS in predicting an unsteady flow field using coarse grids is shown.
  - An extensive static validation is performed in Ref. [12], and a further investigation of the PANS dynamic

simulation is performed analyzing forces and time history velocity signals compared with well-resolved LES results.

- A study of the effect of a dynamic movement of a generic truck cabin is investigated.
  - The flow field of the dynamic configuration is fundamentally different when compared to the quasi-static analysis.
  - The inertia of the flow due to the movement of the model recreates a hysteresis of the C_d and C_s signal.
  - The oscillation is beneficial for the aerodynamic performance. The rotation breaks the large structures of a separated flow. This defines the higher drag observed in the quasi-static configuration.

- The effects of the actuation on the dynamic case are studied.
  - The flow is stabilized by the AFC. The hysteresis of the C_d signal is reduced, and the hysteresis of the C_s is almost suppressed.
  - A C_d reduction is observed for every yaw angle swept by the rotation.
  - The strong influence of the oscillation is mitigated both on the lateral surfaces and in the surrounding flow. The flow control is in fact able to recreate a more homogeneous pressure distribution on both sides of the model during the oscillation.

To conclude, PANS is shown to be a good engineering tool to predict challenging flow conditions, preserving the accuracy of the calculation. This opens the possibility for the prediction of industrial aerodynamic flows that require limited computational resources and a good accuracy of the results. The control strategy used here is beneficial for the control of a flow characterized by wind gusts. A significant reduction of drag and a more stable flow were observed, when side force is taken into account. With this in mind, this paper relates to a larger project, which intends to ultimately study the application and the implementation of an AFC solution for a real truck.

References

[1] Girimaji, S. S., Jeong, E., and Srinivasan, R., 2006, "Partially Averaged Navier–Stokes Method for Turbulence: Fixed Point Analysis and Comparison With Unsteady Partially Averaged Navier–Stokes," ASME J. Appl. Mech., 73(3), pp. 422–429.

[2] Basara, B., Krajnovic, S., Girimaji, S., and Pavlovic, Z., 2011, "Near-Wall Formulation of the Partially Averaged Navier Stokes Turbulence Model," AIAA J., 49(12), pp. 2627–2636.

[3] Jeong, E., and Girimaji, S. S., 2010, "Partially Averaged Navier–Stokes (PANS) Method for Turbulence Simulations-Flow past a Square Cylinder," ASME J. Fluids Eng., 132(12), p. 121203.

[4] Lakshmipathy, S., and Girimaji, S. S., 2010, "Partially Averaged Navier–Stokes (PANS) Method for Turbulence Simulations: Flow past a Square Cylinder," ASME J. Fluids Eng., 132(12), p. 121202.

[5] Mirzaei, M., Krajnović, S., and Basara, B., 2015, "Partially-Averaged Navier–Stokes Simulations of Flows around Two Different Ahmed Bodies," Comput. Fluids, 117, pp. 273–286.

[6] Krajnović, S., Minelli, G., and Basara, B., 2016, "Partially-Averaged Navier-Stokes Simulations of Two Bluff Body Flows," Appl. Math. Comput., 272, pp. 692–706.

[7] Krajnović, S., Minelli, G., and Basara, B., 2016, "Partially-Averaged Navier-Stokes Simulations of Flows around Generic Vehicle at Yaw," SAE Paper 2016-01-1586.

[8] Krajnović, S., Lárusson, R., and Basara, B., 2012, "Superiority of PANS Compared to LES in Predicting a Rudimentary Landing Gear Flow With Affordable Meshes," Int. J. Heat Fluid Flow, 37, pp. 109–122.

[9] Ranjan, P., and Dewan, A., 2015, "Partially Averaged Navier Stokes Simulation of Turbulent Heat Transfer From a Square Cylinder," Int. J. Heat Mass Transfer, 89, pp. 251–266.

[10] Ranjan, P., and Dewan, A., 2016, "Effect of Side Ratio on Fluid Flow and Heat Transfer From Rectangular Cylinders Using the PANS Method," Int. J. Heat Fluid Flow, 61, pp. 309–322.

[11] Han, X., Krajnović, S., and Basara, B., 2013, "Study of Active Flow Control for a Simplified Vehicle Model Using the PANS Method," Int. J. Heat Fluid Flow, 42, pp. 139–150.

[12] Minelli, G., Adi Hartono, E., Chernoray, V., Hjelm, L., Krajnović, S., and Basara, B., 2017, "Validation of PANS and Active Flow Control for a Generic Truck Cabin," J. Wind Eng. Ind. Aerodyn., 171, pp. 148–160.

[13] Jakirlic, S., Kutej, L., Unterlechner, P., and Tropea, C., 2017, "Critical Assessment of Some Popular Scale-Resolving Turbulence Models for Vehicle Aerodynamics," SAE Paper No. 2017–01–1532.

[14] Jakirlic, S., 2018, "Scale-Resolving Simulation of an 'on-Road' Overtaking Maneuver Involving Model Vehicles," SAE Paper No. 2018-01-0706.

[15] Schuetz, T. C., 2015, Aerodynamics of Road Vehicles, 5th ed., SAE International, Warrendale, PA.

[16] Cho, M., Choi, S., and Choi, H., 2016, "Control of Flow Separation in a Turbulent Boundary Layer Using Time-Periodic Forcing," ASME J. Fluids Eng., 138(10), p. 101204.

[17] Gad-el Hak, M., Pollard, A., and Bonnet, J. P., 1998, "Flow Control: Fundamentals and Practices," Flow Control: Fundamentals and Practices, Vol. 53, Springer-Verlag, Berlin.

[18] Glezer, A., Amitay, M., and Honohan, A. M., 2005, "Aspects of Low- and High-Frequency Actuation for Aerodynamic Flow Control," AIAA J., 43(7), pp. 1501–1511.

[19] Woo, G. T. K., and Glezer, A., 2010, "Transitory Control of Dynamic Stall on a Pitching Airfoil," Numer. Fluid Mech. Multidiscip. Des., 108, pp. 3–18.

[20] Yen, J., and Ahmed, N. A., 2012, "Parametric Study of Dynamic Stall Flow Field With Synthetic Jet Actuation," ASME J. Fluids Eng., 134(7), p. 071106.

[21] Gad, L., and Avraham, S., 2014, "Flow Control Applied to the Front Rounded Edge of a Bluff Body," Int. J. Flow Control, 6(1), pp. 21–42.

[22] Lubinsky, G., and Seifert, A., 2014, "Suction and Oscillatory Blowing Applied to the Rounded Front Edges of a Square Prism BT," International Conference on Instability and Control of Massively Separated Flows, Prato, Italy, Sept. 4–6, 2013, pp. 157–162.

[23] Seifert, A., Dayan, I., Horrell, C., Grossmann, J., and Smith, A., 2016, Heavy Trucks Fuel Savings Using the SaOB Actuator BT—The Aerodynamics of Heavy Vehicles—Part III: Trucks, Buses and Trains, Springer International Publishing, Cham, Switzerland, pp. 377–390.

[24] Vernet, J. A., Örlü, R., and Alfredsson, P. H., 2015, "Separation Control by means of Plasma Actuation on a Half Cylinder Approached by a Turbulent Boundary Layer," J. Wind Eng. Ind. Aerodyn., 145, pp. 318–326.

[25] Michelis, T., and Kotsonis, M., 2015, "Flow Control on a Transport Truck Side Mirror Using Plasma Actuators," ASME J. Fluids Eng., 137(11), p. 111103.

[26] Minelli, G., Krajnović, S., Basara, B., and Noack, B. R., 2016, "Numerical Investigation of Active Flow Control around a Generic Truck A-Pillar," Flow, Turbul. Combust., 97(4), pp. 1235–1254.

[27] Minelli, G., Hartono, E. A., Chernoray, V., Hjelm, L., and Krajnović, S., 2017, "Aerodynamic Flow Control for a Generic Truck Cabin Using Synthetic Jets," J. Wind Eng. Ind. Aerodyn., 168, pp. 81–90.

[28] Garry, K. P., and Cooper, K. R., 1986, "Comparison of Quasi-Static and Dynamic Wind Tunnel Measurements on Simplified Tractor-Trailer Models," J. Wind Eng. Ind. Aerodyn., 22(2–3), pp. 185–194.

[29] Krajnović, S., Bengtsson, A., and Basara, B., 2011, "Large Eddy Simulation Investigation of the Hysteresis Effects in the Flow around an Oscillating Ground Vehicle," ASME J. Fluids Eng., 133(12), p. 121103.

[30] Guilmineau, E., and Chometon, F., 2008, "Numerical and Experimental Analysis of Unsteady Separated Flow Behind an Oscillating Car Model," SAE Int. J. Passenger Cars Mech. Syst., 1(1), pp. 646–657.

[31] Watkins, S., and Saunders, J. W., 1995, "Turbulence Experienced by Road Vehicles Under Normal Driving Conditions," SAE Paper No. 1995-02-01.

[32] Wordley, ., and Saunders, J., 2008, "On-Road Turbulence," SAE Int. J. Passenger Cars Mech. Syst., 1(1), pp. 341–360.

[33] Wordley, S., and Saunders, J., 2009, "On-Road Turbulence—Part 2," SAE Int. J. Passenger Cars Mech. Syst., 2(1), pp. 111–137.

[34] AVL, 2014, "Fire Manual v2014," AVL LIST GmbH, Graz, Austria.

[35] Pope, S. B., 2001, Turbulent Flows, Cambridge University Press, Cambridge, UK.

[36] Piomelli, U., and Chasnov, J., 1996, Large-Eddy Simulations: Theory and Applications (ERCOFTAC Series), M. Hallbäck, D. S. Henningson, A. V. Johansson, P. H. Alfredsson, eds., Vol. 2. Springer, Dordrecht, the Netherlands.

[37] Przulj, V., and Basara, B., 2001, "Bounded Convection Schemes for Unstructured Grids," AIAA Paper No. 2001-2593.

[38] Sweby, P. K., 1984, "High Resolution Schemes Using Flux Limiters for Hyperbolic Conservation Laws," SIAM J. Numer. Anal., 21(5), pp. 995–1011.

[39] Harten, A., 1997, "High Resolution Schemes for Hyperbolic Conservation Laws," J. Comput. Phys., 135(2), pp. 260–278.

[40] Girimaji, S. S., 2006, "Partially-Averaged Navier–Stokes Model for Turbulence: A Reynolds-Averaged Navier–Stokes to Direct Numerical Simulation Bridging Method," ASME J. Appl. Mech., 73(3), pp. 413–421.

[41] Germano, M., 1992, "Turbulence: The Filtering Approach," J. Fluid Mech., **238**(1), pp. 325–336.

[42] Ma, J. M., Peng, S. H., Davidson, L., and Wang, F. J., 2011, "A Low Reynolds Number Variant of Partially-Averaged Navier–Stokes Model for Turbulence," Int. J. Heat Fluid Flow, **32**(3), pp. 652–669.

[43] Basara, B., Krajnović, S., and Girimaji, S., 2010, "PANS Methodology Applied to Elliptic-Relaxation Based Eddy Viscosity Transport Model," *Turbulence and Interactions*, Springer, Berlin, pp. 63–69.

[44] Girimaji, S., and Abdol-Hamid, K., 2005, "Partially Averaged Navier-Stokes Model for Turbulence: Implementation and Validation," AIAA Paper 2005-502.

[45] Smagorinsky, J., 1963, "General Circulation Experiments With the Primitive Equations," Mon. Weather Rev., **91** (3), pp. 99–165.

[46] Krajnović, S., 2009, "Large Eddy Simulation of Flows Around Ground Vehicles and Other Bluff Bodies," Philos. Trans. Ser. A, , **367**(1899), pp. 2917–2930.